

High-Sensitivity Microthermometry Method Based on Vacuum-Deposited Thin Films Exhibiting Gradual Spin Crossover above Room Temperature

Oleksandr Ye. Horniichuk, Karl Ridier, Lijun Zhang, Yuteng Zhang, Gábor Molnár, Lionel Salmon, Azzedine Bousseksou

▶ **To cite this version:**

Oleksandr Ye. Horniichuk, Karl Ridier, Lijun Zhang, Yuteng Zhang, Gábor Molnár, et al.. High-Sensitivity Microthermometry Method Based on Vacuum-Deposited Thin Films Exhibiting Gradual Spin Crossover above Room Temperature. ACS Applied Materials & Interfaces, 2022, 14 (46), pp.52140-52148. 10.1021/acsami.2c13834 . hal-03853995

HAL Id: hal-03853995
https://hal.science/hal-03853995

Submitted on 15 Nov 2022

HAL is a multi-disciplinary open access archive for the deposit and dissemination of scientific research documents, whether they are published or not. The documents may come from teaching and research institutions in France or abroad, or from public or private research centers.

L'archive ouverte pluridisciplinaire **HAL**, est destinée au dépôt et à la diffusion de documents scientifiques de niveau recherche, publiés ou non, émanant des établissements d'enseignement et de recherche français ou étrangers, des laboratoires publics ou privés.

High sensitivity microthermometry method based on vacuum-deposited thin films exhibiting gradual spin crossover above room temperature

Oleksandr Ye. Horniichuk,[ab] Karl Ridier,[a] Lijun Zhang,[a] Yuteng Zhang,[a] Gábor Molnár,[a] Lionel Salmon,*[a] Azzedine Bousseksou*[a]

[a] *LCC, CNRS and Université de Toulouse (UPS, INP) 205 route de Narbonne, F-31077 Toulouse, France.*

[b] *Taras Shevchenko National University of Kyiv, Faculty of Chemistry, 12, Lva Tolstogo str., 01033, Kyiv, Ukraine.*

Email: lionel.salmon@lcc-toulouse.fr, azzedine.bousseksou@lcc-toulouse.fr

Abstract. We report on the fabrication, characterization and microthermometry application of high-quality, nanometric thin films, with thicknesses in the range of 20-200 nm, of the molecular spin-crossover complex [Fe(HB(1,2,3-triazol-1-yl)$_3$)$_2$]. The films were obtained by vacuum thermal evaporation and characterized by X-ray diffraction, UV spectrophotometry and atomic force microscopy. The as-deposited films are dense and crystalline with a preferred [011] orientation of the monoclinic crystal lattice normal to the substrate surface. The films exhibit a gradual spin conversion centred at *ca.* 374 K spanning the 273–473 K temperature range, irrespective of their thickness. When deposited on a microelectronic device, these films can be used to enhance the UV-light thermoreflectance coefficient of reflective surfaces by more than an order of magnitude, allowing for high-sensitivity thermoreflectance thermal imaging.

Keywords: spin crossover, vacuum thermal evaporation, thin films, thermoreflectance imaging, microthermometry

1. Introduction

With the continuous advancement of micro- and nanotechnologies, the development of non-invasive thermometry techniques, capable of measuring and imaging the temperature at the micro- and nanoscale, is of paramount importance for various technological fields, such as photonics, microelectronics and biomedicine.[1–9] The most common, industry standard, thermal imaging methods rely on optical thermometry techniques, which consist in tracking an optical response (Planck blackbody emission,[10–12] Raman scattering,[4] luminescence[13] or optical

reflectivity[14–17]) of the investigated object/surface to a temperature change.[1] Importantly, an extension to these conventional thermo-optical techniques can be provided by deposition of temperature-sensitive materials on the investigated surface, such as liquid crystals[18] or luminophores,[9,13,19–23] in order to enhance the thermally-induced optical contrast of the surface, and then the achievable thermal sensitivity and the accuracy of the temperature measurement.

In this context, molecular spin-crossover (SCO) compounds constitute an attractive class of thermoresponsive materials. These transition metal complexes, which can reversibly switch between their low-spin (LS) and high-spin (HS) electronic configurations, exhibit drastic alterations of their optical properties (absorption coefficient, refractive index) under the effect of a temperature change.[24–26] Depending on the crystal packing and/or the strength of the intermolecular interactions in the material, a variety of thermal SCO behaviours have been reported, from very gradual conversions over a wide temperature range, to abrupt transitions, with or without thermal hysteresis loop (memory effect).[27] Interestingly, these different possible characteristics of the thermal spin transition enable various thermometric and thermal imaging approaches, thus providing an appealing scope for thermometry (see Figure 1).[28] (*N.B.* It is worth noting that this type of classification of thermometry approaches also applies to other classes of phase-change materials as well, such as liquid crystals.)

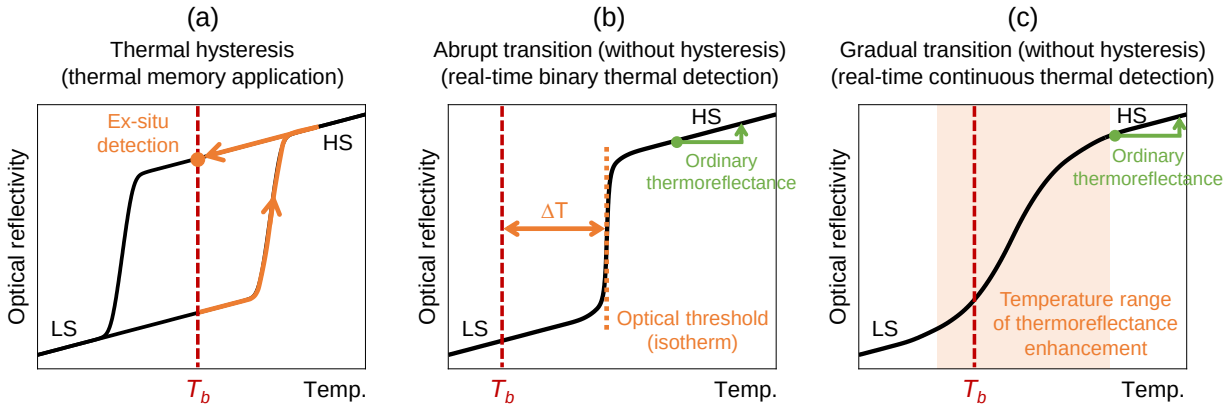


Fig. 1. Schematic representation of the thermal evolution of the optical reflectivity of a SCO thin film, showing that different possible thermometric applications can be envisioned depending on the characteristics of the thermal spin transition of the film: **(a)** thermal memory application (transition with thermal hysteresis), **(b)** real-time binary thermal sensing (abrupt transition without hysteresis) and **(c)** real-time continuous thermal sensing (gradual transition without hysteresis). T_b refers to the base (ambient) temperature of the device under study.

As shown in Figure 1a, and as already demonstrated experimentally,[29] a SCO thin film exhibiting a thermal hysteresis loop can be used to detect *ex situ* the overshoot of a certain threshold temperature, thus allowing for thermal memory application. As the thermally induced optical changes can be read out *a posteriori*, the key interest here is that the temperature

distribution can be mapped using slow and high-resolution imaging methods, such as scanning probe microscopies,[30] to probe fast and spatially localized transient thermal events, which would be hardly detectable using conventional, real-time optical methods.

On the contrary, the absence of thermal hysteresis loop allows for real-time thermometry. Interestingly, different applications can be envisioned depending on the abruptness of the thermal spin transition. For instance, the use of a SCO film with an abrupt thermal transition (ΔT < 10 K) allows a binary detection of the surface temperature, since a brusque change of the optical reflectivity occurs at the transition temperature, bringing out a well-defined isotherm (Figure 1b). This approach was recently demonstrated using the SCO complex [Fe(HB(1,2,4-triazol-1-yl)$_3$)$_2$] which displays an abrupt spin transition centered at 337 K.[31] A great advantage of this approach is that real-time contour maps of the surface temperature distribution can be achieved without any prior thermal calibration of surface properties. Moreover, we have shown that this binary thermal detection method can also afford for high-resolution surface temperature maps, which can be obtained by scanning the base (ambient) temperature T_b of the device under study (controlled with a heating/cooling stage).[31] However, these surface temperature maps cannot be acquired in real time (since it requires to scan the base temperature of the heating device).

Finally, as shown in Figure 1c, another method would consist in using a thin film with a gradual thermal SCO and to carry out conventional thermoreflectance measurements, allowing a continuous and real-time monitoring of the absolute temperature of the surface, provided that a careful thermal calibration of the optical reflectivity is performed beforehand. In this case, the main interest of the SCO film would be to amplify the thermally induced change of the reflectivity of the surface and then to enhance the achievable thermal sensitivity (i.e., the thermoreflectance coefficient). Up to now, however, no thermoreflectance-based thermal imaging method utilizing *gradual* SCO is reported, mainly due to the lack of appropriate samples. Indeed, for this application, the need arises for high-quality, dense, homogeneous SCO thin films displaying a fully reproducible, hysteresis-free, gradual spin conversion above room temperature, capable of withstanding long-term thermal cycling, and exhibiting an overall large thermally induced change of optical reflectivity.

In this work, we demonstrate that the molecular SCO complex [Fe(HB(1,2,3-triazol-1-yl)$_3$)$_2$] **1** (see molecular and crystal structures, Fig. S1),[32] fulfills the above-mentioned conditions and can then be used as an accurate, continuous surface temperature sensor, probed by optical reflectivity. Indeed, contrary to its structural isomer [Fe(HB(1,2,4-triazol-1-yl)$_3$)$_2$] which was used in a previous work as a binary temperature sensor,[31] the polycrystalline bulk

powder of **1** presents a stable, gradual spin transition centred at around 373 K, spanning over a wide temperature range (*ca.* 320–430 K).[32] Here, we show that the complex **1** is sublimable and can be deposited in the form of high-quality, homogeneous thin films by vacuum thermal evaporation, in which the SCO properties are retained. The structural, morphological and electronic properties of the films were investigated using grazing-incidence X-ray diffraction (GIXRD), atomic force microscopy (AFM) and variable-temperature ultraviolet-visible (UV-Vis) spectrophotometry. For surface thermal imaging purposes, Joule-heated metallic microwires, fabricated on top of glass and silicon substrates, were coated with nanometric films of **1**, and their response to local temperature changes was probed by optical reflectivity.

2. Experimental

2.1. Thin film fabrication and characterization

Thin films of **1** were obtained by means of thermal evaporation in a PREVAC thermal deposition system at a base pressure of *ca.* 9×10^{-7} mbar. The bulk powder of the complex, synthesized as reported in refs. 32 and 33, was heated at 210 °C in a quartz crucible and evaporated at a rate of 0.04 Å s^{-1}. The film thickness and the evaporation rate were followed *in situ* using a quartz crystal microbalance. The thickness of the films was verified *ex situ* by spectral reflectance measurements (F20, Filmetrics) and by AFM (SmartSPM, Horiba). The films were deposited onto crystalline silicon (100 orientation) and amorphous fused silica substrates, which were cleaned beforehand *via* 5 min sonication in acetone and ethanol.

The GIXRD experiments were carried out in ambient conditions by means of a PANalytical X'Pert PRO MPD system using Cu-Kα radiation (45 kV and 40 mA) and a parallel-beam configuration. The incident beam optics consisted of a mirror with a 1/32° divergence slit. A parallel plate collimator (0.18°) and Soller slits (0.04°) were mounted on the path of the diffracted beam. An X'Celerator detector in receiving slit mode was used for X-ray collection. AFM surface topography analysis was conducted in amplitude-modulation mode at room temperature using the SmartSPM. The temperature-dependent absorbance spectra of the thin films were collected at wavelengths between 200 and 600 nm using a Cary 50 (Agilent Technologies) spectrophotometer and a Linkam FTIR-600 heating-cooling stage. The sample chamber was purged with dry nitrogen and spectra were acquired in the 253–453 K range with 2 K min^{-1} rate.

2.2. Microthermometry experiments

Gold microwires (length 1–2 mm, thickness 250 nm and width 2–16 μm) were patterned on glass and thermally oxidized silicon substrates by a photolithography method, as reported

earlier.[29,31,34] The substrates (and the microwires) were then coated with a 120-nm-thick film of **1** by vacuum thermal evaporation. The SCO-coated chip was connected to a source-meter (Keithley 2611A) *via* an eight-track connector[31] and mounted on a variable-temperature microscope stage (Linkam Scientific Instruments, LTS120) to control the base temperature (T_b) of the entire circuit. The microwire electrical characterizations and operation were carried out by applying current and not voltage bias in order to guarantee a reproducible Joule heating. Optical reflectivity images were recorded at λ = 310 nm (LED source) and λ = 452 nm (halogen lamp with a spectral range reduced by a band-pass filter) using a custom-made optical microscope (compatible with UV light) equipped with a ×5 magnification objective (numerical aperture, NA= 0.12) and a CCD camera (Andor Technology Clara, 1392 × 1040 pixels of 6.45 µm size).

3. Results and discussion

3.1. Fabrication and characterization of [Fe(HB(1,2,3-triazol-1-yl)$_3$)$_2$] films

Thin films of **1** were deposited by vacuum thermal evaporation with thicknesses in the 20–200 nm range. The X-ray diffraction patterns of the films reveal an intense peak at 2θ = 12.15° (Fig. 2a) that points to crystallinity and preferential crystallographic orientation of the as-deposited films. Fig. 2a also shows the diffraction pattern of the microcrystalline bulk powder, which displays a similar peak at 2θ = 12.09°. In the simulated PXRD pattern of **1**[32] this peak corresponds to the 011 reflection. We can thus suggest that crystallites in the films grow preferentially with the [011] direction of the monoclinic unit cell normal to the substrate surface. This observation was systematically confirmed, irrespective of the substrate material (silicon or fused silica) and the film thickness. The diffractograms did not undergo significant changes upon long-term storage (months) of the films in ambient conditions. It is interesting to note here that the complex [Fe(HB(1,2,4-triazol-1-yl)$_3$)$_2$], which is the structural isomer of **1**, forms an amorphous film upon vacuum thermal deposition and only a subsequent solvent vapor annealing affords for the formation of a textured, crystalline film.[35] The 011 diffraction peak intensity of the as-deposited films of **1** correlates with the thickness, indicating a similar degree of crystallinity and texture for each film in the investigated thickness range (Fig. 2b). From the width of the 011 diffraction peak, the average size of the coherent crystalline domains can be calculated using the Scherrer equation.[36] As for the absolute values, care must be taken because the peak widths were corrected for instrument broadening, but not for other possible effects, such as micro-strain. Nevertheless, the tendency shown in Figure 2c clearly evidences that the size of the crystalline domains grows steadily with the film thickness.

Representative AFM surface topography data of films of **1** with different thicknesses, deposited on fused silica substrates, are shown in Figure 3. The nanocrystalline surface morphology of the films is obvious with RMS roughness values typically between 7 and 11 nm. The particle morphology does not substantially depend on the film thickness or the nature of the substrate (see Fig. S2), but one can notice a more dense packing in the thicker films.

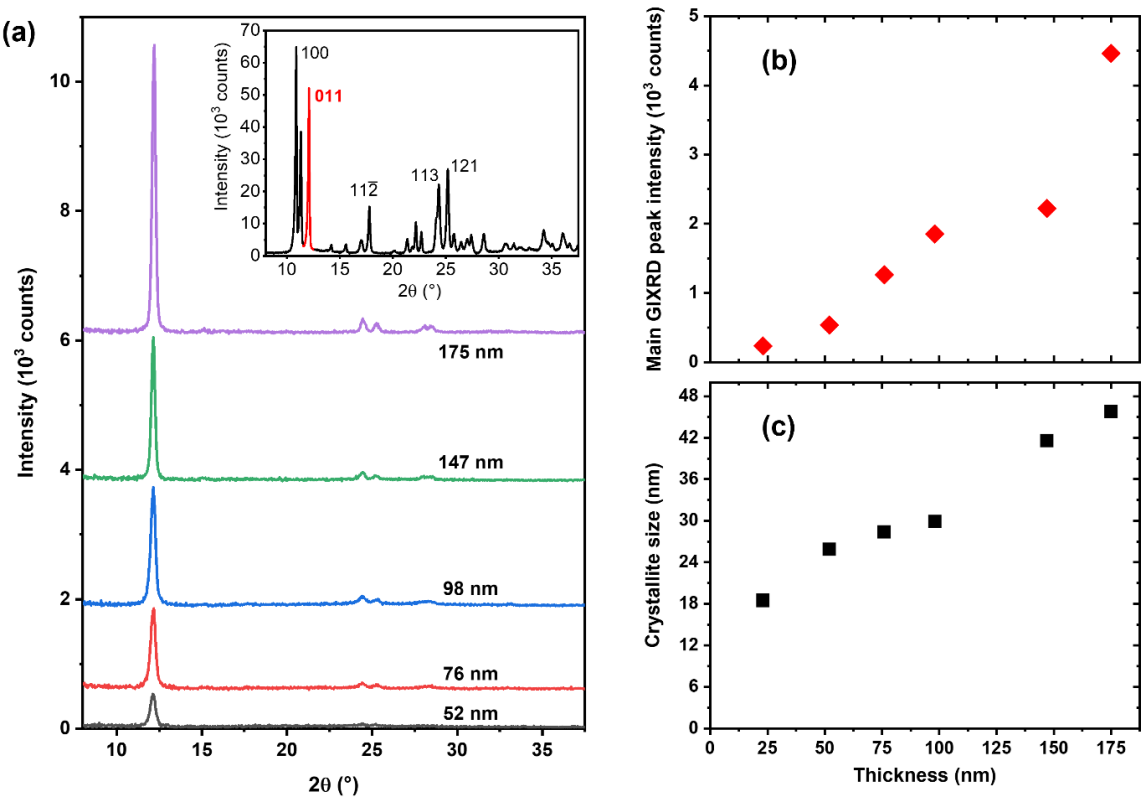


Fig. 2. Crystallinity of the films. (a) XRD patterns of nanocrystalline thin films of **1** with various thicknesses, deposited on Si substrates. The inset shows the XRD pattern of the microcrystalline powder of **1**. **(b)** Intensity of the 011 reflection as a function of the film thickness. **(c)** Average size of the crystalline domains (calculated for the 011 reflection using the Scherrer method) as a function of the film thickness.

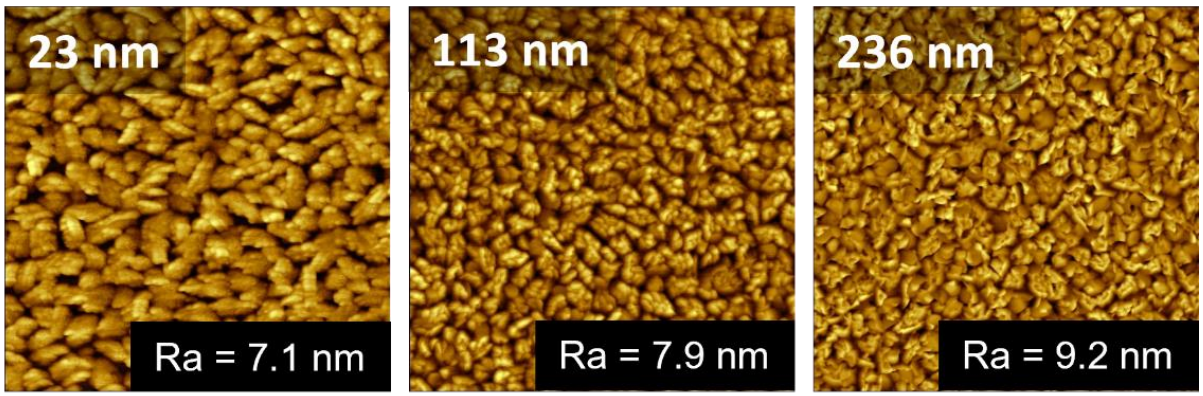


Fig. 3. Morphology of the films. Representative AFM topography images of films of **1** with different thicknesses (23, 113 and 236 nm) deposited on silicon substrates. The scan size is 5 × 5 μm^2.

In order to investigate the SCO properties in the thin films of **1**, variable-temperature UV-vis spectrophotometry measurements were conducted over three to eight heating-cooling cycles between 253 and 453 K at 2 K min^{-1} rate. The measurements were performed for the films deposited on transparent fused silica substrates. The room-temperature absorbance spectra of the films display three absorption bands with maxima at 208, 275 and 336 nm (Fig. 4a). The absorbance level of these bands decreases upon heating, while a fourth band appears at 230 nm and exhibits higher absorbance at high temperatures (Fig. 4a). As a result, the variable temperature spectra are characterized by two isosbestic points at *ca.* 220 and 260 nm. Taking into account the high absorption coefficients associated with these peaks, we can safely assign them to charge transfer (metal-to-ligand and/or ligand-to-metal) transitions.

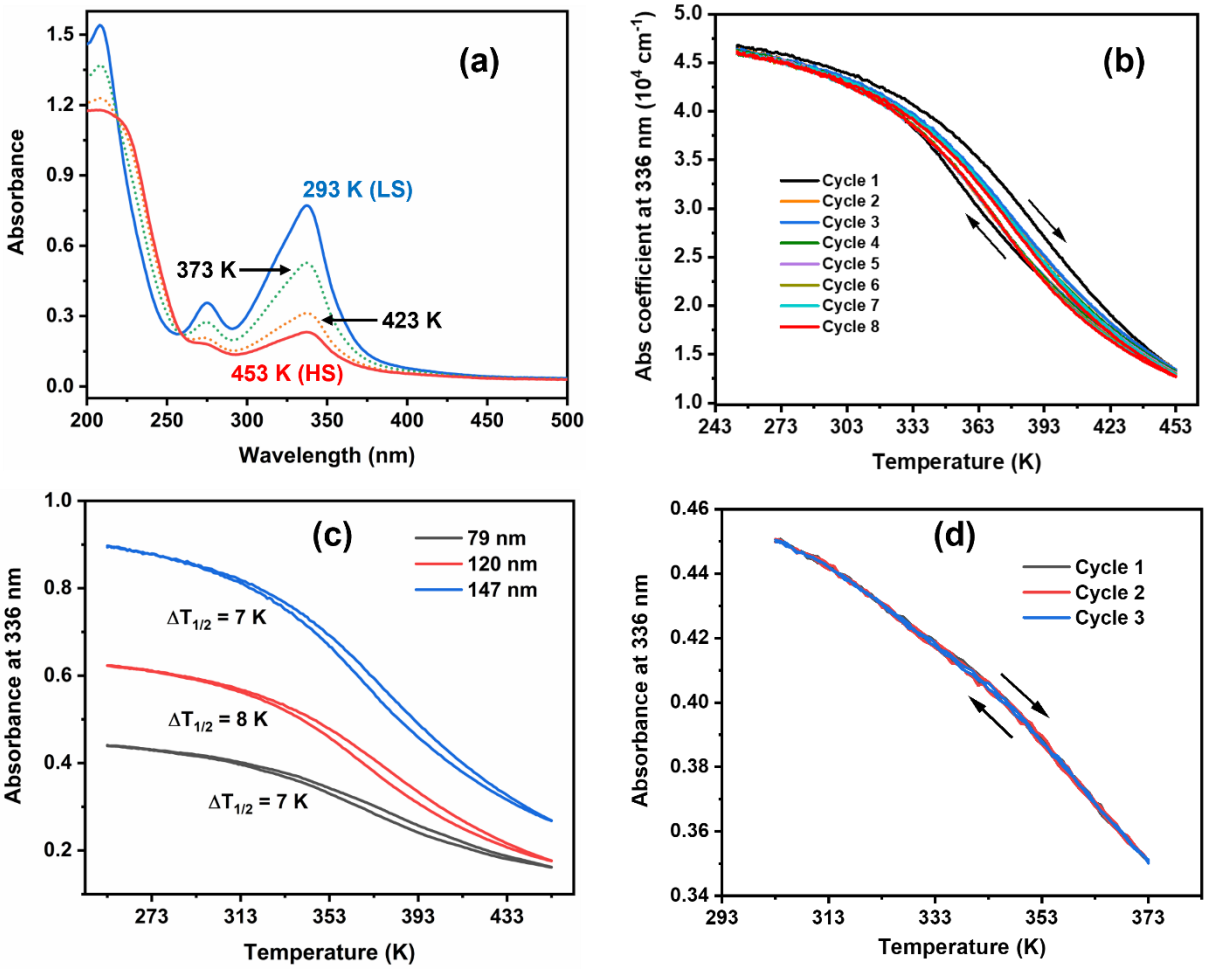


Fig. 4. SCO properties of the films. (a) Optical absorbance spectra of a 175-nm-thick film of **1** on fused silica substrate, acquired at selected temperatures. **(b)** Temperature dependence of the absorbance at 336 nm of the same 175-nm film upon eight heating-cooling cycles between 253 and 453 K. **(c)** Thermal variation of the absorbance at 336 nm for a 79, 120 and 147-nm-thick film of **1** upon heating-cooling cycles between 253 and 453 K. **(d)** Thermal variation of the optical absorbance at 336 nm for a 79-nm-thick film of **1** upon three heating-cooling cycles from 303 to 373 K.

We use the thermal evolution of the highest intensity absorption band at 336 nm to follow the occurrence of a spin-state change in the films. Typical transition curves, displayed in Figure 4b, reveal a very gradual spin conversion between the LS and HS states, similar to the one observed in the bulk powder.[32] The transition temperature is centered around 374 ± 2 K, independently of the film thickness (Fig. 4c). The transition is virtually complete at 273 K (pure LS state), whereas a residual LS fraction of *ca.* 5-10 % is still observed at 453 K. (*N.B.* Heating above *ca.* 453 K leads to the degradation of the films.) A notable, unusual characteristic of the SCO in the films of **1** is the occurrence of a thermal hysteresis, which is not expected for such a gradual spin conversion. At the first heating-cooling cycle this thermal hysteresis loop is usually broad reaching up to 35 K in width, while on further cycling it narrows down to *ca.* 7 K. Importantly, we found, however, that reducing the thermal cycling span leads to a narrowing of the hysteresis loop. Indeed, reducing the end temperature from 453 K to 393 K results in a 4-K-wide hysteresis loop, whereas the thermal hysteresis can be completely removed by limiting the heating of the sample to 373 K, leading to perfectly reversible and reproducible spin-transition curves (Fig. 4d and Fig. S3).

To summarize the somewhat unusual SCO properties of the vacuum-deposited films of **1**, we can say that they display a very gradual spin conversion between *ca.* 273 and 473 K, similar to that of the bulk powder. Up to *ca.* 373 K (i.e., the half-transition), the SCO is perfectly reversible, without any thermal hysteresis, thus providing scope for real-time thermometry applications. However, when heating above this temperature, a more and more broad thermal hysteresis loop opens. This hysteresis obviously does not refer to the usually encountered cooperative phenomena in SCO materials. Instead, it is likely an indication of small, irreversible changes in the material when cycling at high temperature. Due to this phenomenon, accurate thermal sensing is not possible in the full 373–453 K range, but still it is possible to acquire thermal images. Finally, above *ca.* 453 K, the films start to degrade, presumably due to the sublimation of the molecules. At present, we have no unequivocal explanation for the opening of the thermal hysteresis loop above 373 K. Preliminary AFM and GIXRD data acquired on samples cycled at high temperatures reveal the existence of structural changes in the films as well as a visible modification of their surface morphology (see Fig. S4), but further work will be necessary to reach a clear-cut conclusion.

3.2. Microthermometry application of [Fe(HB(1,2,3-triazol-1-yl)$_3$)$_2$] films

Taking advantage of the above-mentioned properties, we have undertaken experiments to explore the use of thin films of **1** as a temperature sensor, probed by optical reflectivity, for

mapping and measuring the surface temperature through thermoreflectance thermal imaging. Indeed, the role of the SCO film is to enhance the thermoreflectance properties of surfaces in a broad temperature range – especially in the UV spectral domain where a drastic change of the optical absorbance occurs when switching between the LS and HS states; the improved thermoreflectance involving an increased thermally induced change in optical reflectivity and, therefore, a greater thermal sensitivity for measuring the surface temperature.

Figure 5a (top panels) shows the thermal evolution of optical reflectivity, $\Delta R/R = (R - R_{298K})/R_{298K}$, at λ = 310 nm (close to the maximum absorbance wavelength) on SCO-coated (120 nm) and uncoated gold, silicon and glass surfaces. Remarkably, the presence of the SCO layer significantly enhances the thermoreflectance properties of surfaces, providing a relative change of the reflectivity by +29.4 %, +10.4 % and -2.4 % on silicon, gold and glass surfaces, respectively, in the temperature range between 298 and 373 K. By comparison, on uncoated surfaces, these relative changes (ordinary thermoreflectance) remain moderate: +0.9 % on silicon and gold surfaces and -1.1 % on glass. The observed changes are much greater on silicon (and to a lesser extent on gold), which is a reflective surface in the UV range (compared to glass). On these surfaces, the optical reflectivity is found to increase with temperature ($\Delta R/R > 0$), which is compatible with a progressive reduction of the absorbance of the SCO film at this wavelength upon the spin transition. Figure 5a (bottom panels) depicts the thermal evolution of the corresponding thermoreflectance coefficient (κ), defined as $\kappa = \mathrm{d}(\Delta R/R)/\mathrm{d}T$, on the various investigated surfaces (λ = 310 nm). While κ is virtually constant for uncoated surfaces in the temperature range 298–373 K, κ = +0.013 % K^{-1}, +0.012 % K^{-1} and -0.014 % K^{-1} for silicon, gold and glass surfaces, respectively, the thermoreflectance coefficient is not constant on SCO-coated surfaces due to the spin-transition phenomenon. On SCO-coated silicon, κ varies from 0.085 % K^{-1} at 298 K to 0.77 % K^{-1} at 373 K. In other words, the thermoreflectance coefficient (i.e., the thermal sensitivity) is multiplied by 6.5 at 298 K up to a factor of 59 at 373 K due to the presence of the SCO layer. On gold, κ changes from 0.078 % K^{-1} to 0.26 % K^{-1} when heating from 298 to 373 K, which corresponds to an increase of the thermoreflectance coefficient by a factor of 6.5 and 22 at 298 and 373 K, respectively, compared to the pristine gold surface. Finally, the effect is less advantageous on transparent glass substrates where κ changes from -0.050 % K^{-1} to -0.009 % K^{-1} when heating from 298 to 373 K, which means that the thermal sensitivity is increased by a factor 3.6 (in absolute value) at 298 K, but becomes lower than the ordinary thermoreflectance at high temperature. One should note here that further enhancements of the thermoreflectance coefficient can be anticipated, for instance by using a light source matching the wavelength of maximum absorbance (336 nm) and/or by increasing

the thickness of the SCO film. However, in both cases, the price to pay would be an increasing disturbance of the surface temperature caused by the presence of the SCO film (i.e., increased invasiveness), which is particularly detrimental for fast (< ms) temperature monitoring. As with the optical absorbance measurements, it should be noted that no notable difference is observed in these thermal calibration curves between heating and cooling modes (see Fig. S5), which signifies that the performance of the SCO film, in terms of thermal change of the optical reflectivity, is fully reversible in the temperature range 298–373 K.

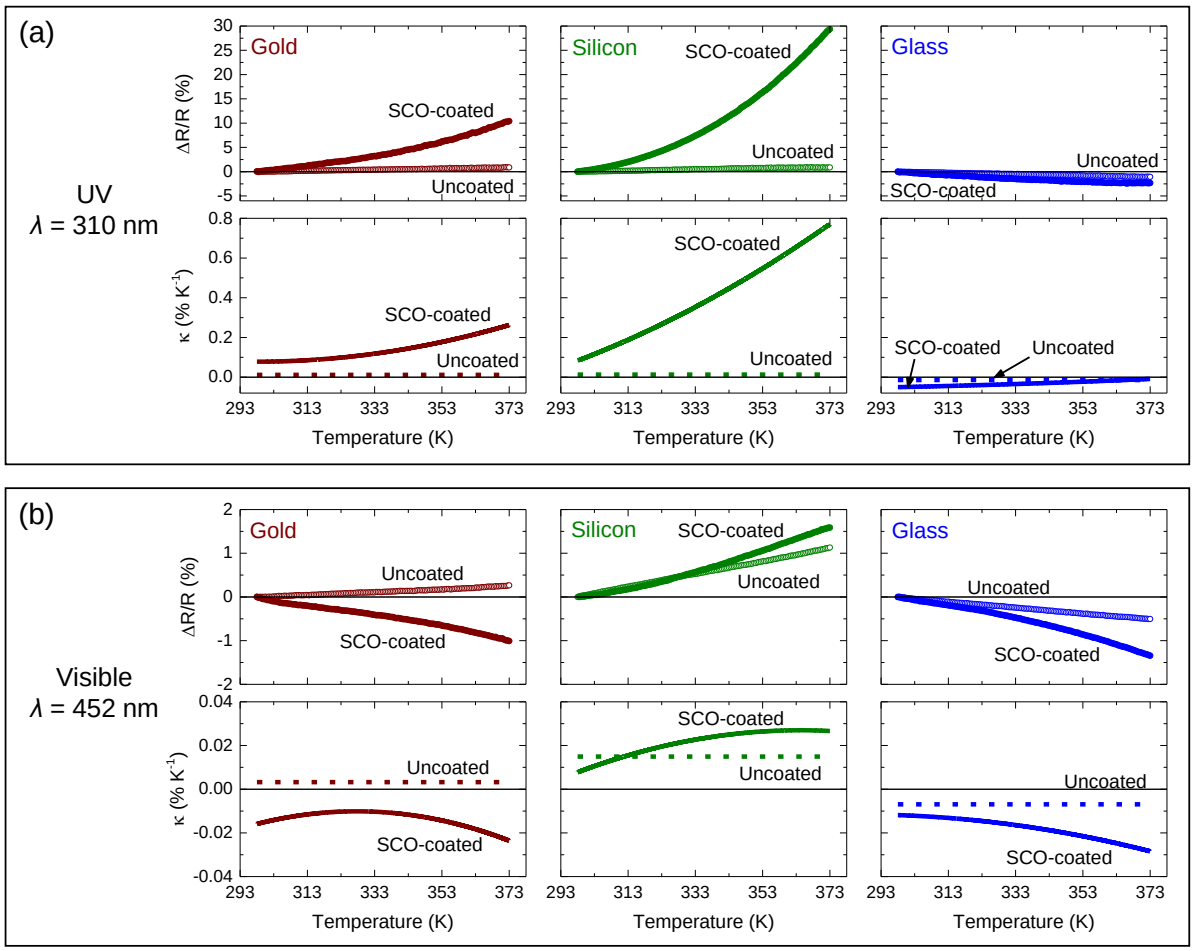


Fig. 5. Thermal calibrations of the optical reflectivity. (a) Thermal evolution of the relative optical reflectivity change, $\Delta R/R = (R–R_{298K})/R_{298K}$, (top panel) and of the corresponding thermoreflectance coefficient, $\kappa = \mathrm{d}(\Delta R/R)/\mathrm{d}T$, (bottom panel) measured at λ = 310 nm on SCO-coated and uncoated surfaces of gold, silicon and glass. **(b)** Thermal evolution of the relative optical reflectivity change, $\Delta R/R$, (top panel) and of the corresponding thermoreflectance coefficient, κ, (bottom panel) measured at λ = 452 nm on SCO-coated and uncoated surfaces of gold, silicon and glass. For each measurement, the surface was heated from 298 to 373 K at a temperature scan rate of 2 K min^{-1}.

Interestingly, as shown in Figure 5b, only a slight improvement of the thermoreflectance properties is evidenced on the SCO-coated surfaces in the visible range (λ = 452 nm), i.e., in a

spectral domain out of the SCO-dependent absorption band of the film. This result indicates that most of the change of the optical reflectivity along the spin transition arises from the variation of the absorption properties of the film, rather than a simple change of the refractive index. On the whole, these measurements show that the presence of the SCO thin film entails a substantial increase of the thermoreflectance properties in the UV range, by more than one order of magnitude compared to the ordinary thermoreflectance, especially on reflective surfaces like gold or silicon, which consequently implies a sizeable enhancement of the sensitivity (in terms of optical reflectivity signal) to any change of the surface temperature.

In order to investigate the potential of this SCO thin film in terms of thermoreflectance thermal imaging, we fabricated a variety of Joule-heated gold microwires (length 1–2 mm, thickness 250 nm) on top of glass and oxidized silicon chips by means of photolithography (see Fig. 6a). The surface of the chips was then entirely covered with a 120-nm-thick film of **1**. Note that due to its insulating nature, the presence of the molecular films of **1** on the surface is not invasive and does not perturb the electrical performance of the device.

Optical reflectivity images (λ = 310 nm) of a SCO-coated microwire (length 2 mm, width 16 µm) on a glass substrate were acquired by optical microscopy at T = 298 K (see Fig. 6b), in both ON ($I \neq 0$) and OFF ($I = 0$) states of the heating device. Figure 6c (left) shows a map of the relative change of optical reflectivity, $\Delta R/R = (R_{ON}–R_{OFF})/R_{OFF}$, following the application of an electrical current of 65 mA in the wire. A strong increase of the optical reflectivity is observed on the wire, and, to a lesser extent on the electrode. On the glass substrate, in the immediate vicinity of the wire, a slight decrease of the reflectivity is also observed, which is compatible with an increase of the temperature following the application of the electrical current. (As indicated in Figure 5a, we remind that the optical reflectivity increases/decreases on gold/glass surface following a temperature rise.) For comparison, the same experiment was performed with an identical microwire on an uncoated, pristine chip. As shown in Figure 6c (right), the variation of optical reflectivity associated with the application of the same electrical current (65 mA) is considerably lower than that observed for the SCO-coated surface, which demonstrates the substantial gain provided by the thermosensitive SCO layer in terms of thermoreflectance properties and, therefore, in terms of thermal sensitivity.

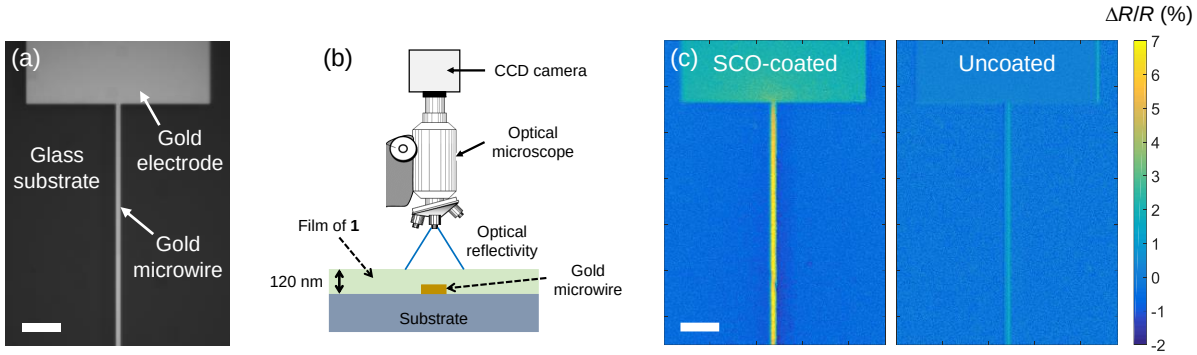


Fig. 6. Thermal sensitivity improvement. (a) Optical reflectivity *R* image of a Joule-heated gold microwire (2-mm-long and 16-µm-wide) on top of a glass substrate. **(b)** Scheme of the experimental setup. **(c)** Relative change of optical reflectivity (λ = 310 nm), $\Delta R/R = (R_{ON}-R_{OFF})/R_{OFF}$, following the application of an electrical current of 65 mA in the wire, for (left) an SCO-coated surface and (right) an uncoated surface. In both cases, the base temperature T_b of the chip was maintained at 298 K. The scale bars are 100 µm.

Taking advantage of this enhanced thermal sensitivity, we were able to deduce accurate temperature maps of the Joule-heated microwires. Indeed, based on the thermal calibration curves of the optical reflectivity shown in Figure 5a, the reflectivity ($\Delta R/R$) map measured in Figure 6c (left) can be easily transformed into a temperature map, by simply converting the measured value of $\Delta R/R$, on each pixel of the image, into a temperature value. As shown in Figure 7, this procedure allowed us to map the temperature field of the surface with a micrometric spatial resolution, for different values of the applied electrical current. As expected, these temperature maps show that the heating is mainly localized on the gold microwire, while a progressive diffusion of heat is also observed into the substrate and the metallic electrode when increasing the electrical current, as already reported in our previous study.[31] (*N.B.* However, it should be noted that the temperature gradients observed on the surrounding glass substrate are less marked than in our previous study[31] mainly because of the use, in the present work, of wider Joule-heating wires (16-µm-wide instead of 1-µm-wide) which generate less pronounced thermal gradients.) From these temperature maps, we can deduce an average temperature of the Joule-heated microwire T_{wire} of 315.9, 320.0, 325.4, 329.9 and 336.6 K for an applied current of 45, 50, 55, 60 and 65 mA, respectively. These values are reported in Figure 8b (open squares).

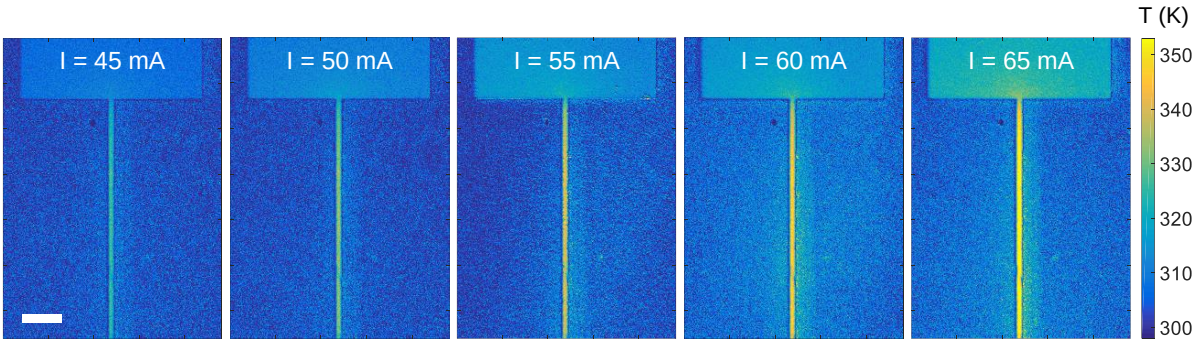


Fig. 7. Quantitative microthermometry. Temperature maps of a SCO-coated, 16-µm-wide gold microwire on top of a glass substrate for various applied electrical currents ranging from 45 to 65 mA (T_b = 298 K). The maps are deduced from the optical reflectivity (λ = 310 nm) images, $\Delta R/R = (R_{ON}–R_{OFF})/R_{OFF}$, of the SCO-coated surface. The pixel size of the temperature maps is 2.6 × 2.6 µm^2. The scale bar is 100 µm.

To validate the results obtained with our SCO-based thermometry technique, we also determined the average temperature of the Joule-heated microwire by measuring its electrical resistance. Indeed, the thermal variation induced by the applied current generates a change of electrical resistance ΔR_Ω, proportional to the mean temperature rise of the wire: $\Delta R_\Omega = \alpha \Delta T_{wire}$. To determine the value of α, a thermal calibration of the resistance of the microwire was performed, by measuring the evolution of R_Ω at low-bias current (5 mA) for various base temperatures (T_b) of the chip. A linear dependence is observed, giving a value of $\alpha = 3.84 \times 10^{-2}\ \Omega\ K^{-1}$ (Fig. 8a). Therefore, in the course of the thermoreflectance measurements, the resistance was simultaneously measured for each value of the applied electrical current, providing a reliable comparative means to monitor in real time the actual average temperature T_{wire} of the Joule-heated wire. Figure 8b summarizes the values of T_{wire} obtained from the two methods for the different applied electrical currents bias, the chip being kept at room temperature (T_b = 298 K). As shown in Figure 8b, and as expected, the temperature of the wire increases with the current following a typical quadratic evolution (Joule effect). Importantly, we notice that the temperature values obtained from these two techniques are in very good agreement, the observed relative difference being typically 2–5 % and always lower than 2 K.

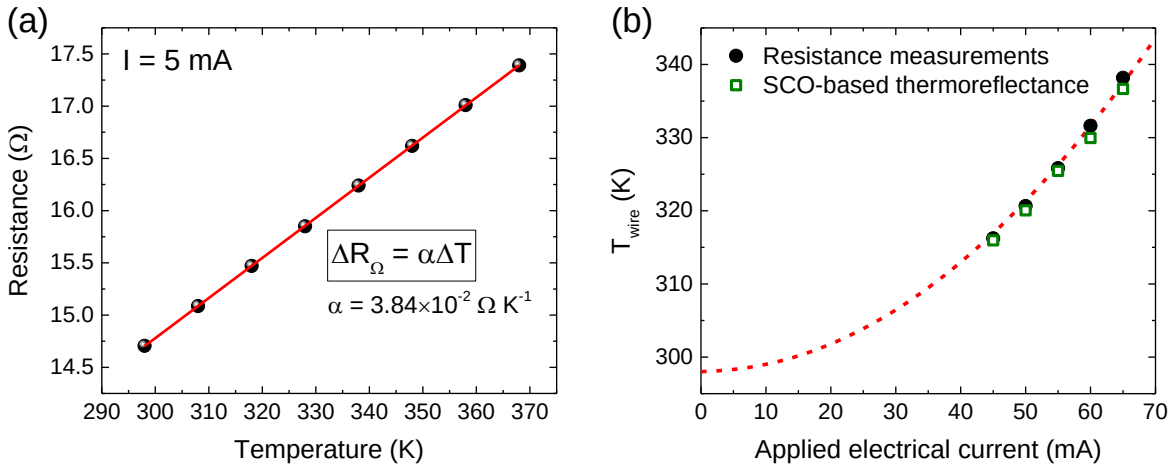


Fig. 8. Comparison with electrical resistance measurements. (a) Variation of the electrical resistance R_Ω of the microwire, measured at low-bias current (5 mA), as a function of the base temperature (T_b) of the substrate, controlled with a variable-temperature stage. The linear temperature coefficient of the wire is $\alpha = 3.84 \times 10^{-2}$ Ω K^{-1}. **(b)** Average temperature of the Joule-heated wire, T_{wire}, for various applied electrical currents ranging from 45 to 65 mA (T_b = 298 K), inferred from SCO-based thermoreflectance thermal imaging (open squares) and from electrical resistance measurements (filled circles). The red dotted line indicates the typical quadratic evolution of the resistance (and thus of the wire temperature) with the applied electrical current.

On the whole, these data demonstrate the possibility of using SCO thin films of **1** for imaging the surface temperature at the micrometric scale with a thermal accuracy of the order of ~1 K (using a simple CCD-based optical detection), by taking advantage of a *ca.* one order of magnitude enhancement of the UV-light thermoreflectance coefficient brought into by the presence of the SCO layer. We have not investigated the ultimate spatial and temporal resolution of our SCO-based thermometer, which would require more sophisticated equipment, but the enhanced thermoreflectance coefficient is obviously a key asset in this context. Furthermore, the fact that the films operate in the UV spectral range is clearly advantageous for imaging sub-micrometer features. For example, a powerful NA = 0.9 microscope objective could provide a 0.35 micron spot imaging at a wavelength of 310 nm. As for the temporal resolution, the limiting factor is the heat diffusion rate in the film, the molecular SCO phenomenon being intrinsically faster.[37] Indeed, due to their low thermal diffusivity, the thermalization process of such SCO films is completed in ~1 µs,[37] which thus defines the accessible temporal resolution of our surface thermometer. Experiments on similar molecular films indicate that a 100-nm-thick film of **1** could potentially afford for temperature measurements down to the µs timescale.[31]

Overall, the thermometric characteristics demonstrated in the present work are virtually comparable to those obtained with the compound [Fe(HB(1,2,4-triazol-1-yl)$_3$)$_2$],[31] in terms of accessible thermal, spatial and temporal resolution. However, it is worth to emphasize that the thermometric approaches used in these two cases are totally different, each having their advantages and disadvantages. The use of [Fe(HB(1,2,4-triazol-1-yl)$_3$)$_2$] (abrupt spin transition) allowed for a binary detection of the surface temperature, working on any surface without the need of thermal calibration procedure of the optical reflectivity. However, in this case, surface temperature maps could not be acquired in real time. Conversely, in this work, we show that the use of compound **1** allows for real-time thermal imaging, based on a prior thermal calibration of the optical reflectivity. However, as the enhancement of the thermoreflectance coefficient induced by the SCO film is surface dependent, this thermometry method is not equally effective on all surfaces.

4. Conclusions

We have fabricated and characterized the structural, morphological and spin-transition properties of vacuum-deposited thin films (20–200 nm) of the molecular SCO complex [Fe(HB(1,2,3-triazol-1-yl)$_3$)$_2$]. These dense, textured, nanocrystalline films are shown to maintain a gradual spin conversion between *ca.* 273 and 473 K, as observed for the bulk powder of this compound. To our best knowledge, this is only the third SCO film, fabricated by thermal evaporation, which displays above-room-temperature SCO and the first, which fulfills requirements for real-time thermal imaging applications on a wide temperature range. We demonstrate that the very gradual spin-state conversion in these films affords for a novel, quantitative, microthermometry approach, wherein the SCO film is used to enhance, in some cases by more than one order of magnitude, the UV-light thermoreflectance coefficient of the coated surface. We show that the key property for this thermal sensitivity gain is the pronounced change of the UV absorbance of the films upon the spin transition.

This work extends the limited portfolio of SCO compounds for demanding microthermometry applications and highlights once again the technological interest of this family of stimuli-responsive molecular materials. Yet, it remains crucial to develop further high-quality thin films and other micro-nano-objects of SCO materials displaying robust, near-room-temperature SCO combined with the desired (optical, electrical, mechanical) functionalities[38–41].

Supporting Information: molecular and crystal structure for [Fe(HB(1,2,3-triazol-1-yl)$_3$)$_2$], AFM topography images, thermal variation of the optical absorbance and optical reflectivity, grazing-incidence X-ray diffraction patterns.

Acknowledgements

OYH acknowledges the French Embassy in Ukraine and Campus France for a BGF scholarship.

References

(1) Kim, M. M.; Giry, A.; Mastiani, M.; Rodrigues, G. O.; Reis, A.; Mandin, P. Microscale Thermometry: A Review. *Microelectron. Eng.* **2015**, *148*, 129–142. https://doi.org/10.1016/j.mee.2015.11.002.

(2) Brites, C. D. S.; Lima, P. P.; Silva, N. J. O.; Millán, A.; Amaral, V. S.; Palacio, F.; Carlos, L. D. Thermometry at the Nanoscale. *Nanoscale* **2012**, *4* (16), 4799–4829. https://doi.org/10.1039/c2nr30663h.

(3) Mecklenburg, M.; Hubbard, W. A.; White, E. R.; Dhall, R.; Cronin, S. B.; Aloni, S.; Regan, B. C. Nanoscale Temperature Mapping in Operating Microelectronic Devices. *Science (80-.).* **2015**, *347* (6222), 629–632. https://doi.org/10.1126/science.aaa2433.

(4) Zani, V.; Pedron, D.; Pilot, R.; Signorini, R. Contactless Temperature Sensing at the Microscale Based on Titanium Dioxide Raman Thermometry. *Biosensors* **2021**, *11* (4), 102. https://doi.org/10.3390/bios11040102.

(5) Jauffred, L.; Samadi, A.; Klingberg, H.; Bendix, P. M.; Oddershede, L. B. Plasmonic Heating of Nanostructures. *Chem. Rev.* **2019**, *119* (13), 8087–8130. https://doi.org/10.1021/acs.chemrev.8b00738.

(6) Chen, C.; Shen, T.; Du, Z.; Zhang, J.; Wang, J.; Marconnet, A.; Pan, L. Microscale Two-Dimensional (2D) Temperature Mapping by Ratiometric Fluorescence Imaging under Orthogonal Excitations. *Exp. Therm. Fluid Sci.* **2018**, *94* (May 2017), 168–171. https://doi.org/10.1016/j.expthermflusci.2018.02.009.

(7) Mykhaylyk, V.; Kraus, H.; Zhydachevskyy, Y.; Tsiumra, V.; Luchechko, A.; Wagner, A.; Suchocki, A. Multimodal Non-Contact Luminescence Thermometry with Cr-Doped Oxides. *Sensors* **2020**, *20* (18), 5259. https://doi.org/10.3390/s20185259.

(8) Ghifari, N.; Rassouk, S.; Hayat, Z.; Taleb, A.; Chahboun, A.; El Abed, A. I. Dye-Doped ZnO Microcapsules for High Throughput and Sensitive Optofluidic Micro-Thermometry. *Micromachines* **2020**, *11* (1), 100. https://doi.org/10.3390/mi11010100.

(9) Rocha, J.; Brites, C. D. S.; Carlos, L. D. Lanthanide Organic Framework Luminescent

Thermometers. *Chem. - A Eur. J.* **2016**, *22* (42), 14782–14795. https://doi.org/10.1002/chem.201600860.

(10) Teyssieux, D.; Thiery, L.; Cretin, B. Near-Infrared Thermography Using a Charge-Coupled Device Camera: Application to Microsystems. *Rev. Sci. Instrum.* **2007**, *78* (3), 034902. https://doi.org/10.1063/1.2714040.

(11) Fletcher, D. THERMAL MICROSCOPY WITH A MICROFABRICATED SOLID IMMERSION LENS. *Microscale Thermophys. Eng.* **2003**, *7* (4), 267–273. https://doi.org/10.1080/10893950390245985.

(12) Kenneth E. Goodson and Mehdi Ashegh. NEAR-FIELD OPTICAL THERMOMETRY. *Microscale Thermophys. Eng.* **1997**, *1* (3), 225–235. https://doi.org/10.1080/108939597200241.

(13) Jaque, D.; Vetrone, F. Luminescence Nanothermometry. *Nanoscale* **2012**, *4* (15), 4301–4326. https://doi.org/10.1039/c2nr30764b.

(14) Tessier, G.; Bardoux, M.; Boué, C.; Filloy, C.; Fournier, D. Back Side Thermal Imaging of Integrated Circuits at High Spatial Resolution. *Appl. Phys. Lett.* **2007**, *90* (17), 171112. https://doi.org/10.1063/1.2732179.

(15) Christofferson, J.; Maize, K.; Ezzahri, Y.; Shabani, J.; Wang, X.; Shakouri, A. Microscale and Nanoscale Thermal Characterization Techniques. *J. Electron. Packag.* **2008**, *130* (4), 041101–041106. https://doi.org/10.1115/1.2993145.

(16) Cahill, D. G.; Ford, W. K.; Goodson, K. E.; Mahan, G. D.; Majumdar, A.; Maris, H. J.; Merlin, R.; Phillpot, S. R. Nanoscale Thermal Transport. *J. Appl. Phys.* **2003**, *93* (2), 793–818. https://doi.org/10.1063/1.1524305.

(17) Christofferson, J.; Shakouri, A. Thermoreflectance Based Thermal Microscope. *Rev. Sci. Instrum.* **2005**, *76* (2), 024903. https://doi.org/10.1063/1.1850632.

(18) Csendes, A.; Székely, V.; Rencz, M. Thermal Mapping with Liquid Crystal Method. *Microelectron. Eng.* **1996**, *31* (1–4), 281–290. https://doi.org/10.1016/0167-9317(95)00350-9.

(19) Zhou, J.; del Rosal, B.; Jaque, D.; Uchiyama, S.; Jin, D. Advances and Challenges for Fluorescence Nanothermometry. *Nat. Methods* **2020**, *17* (10), 967–980. https://doi.org/10.1038/s41592-020-0957-y.

(20) van Swieten, T. P.; van Omme, T.; van den Heuvel, D. J.; Vonk, S. J. W.; Spruit, R. G.; Meirer, F.; Garza, H. H. P.; Weckhuysen, B. M.; Meijerink, A.; Rabouw, F. T.; Geitenbeek, R. G. Mapping Elevated Temperatures with a Micrometer Resolution Using the Luminescence of Chemically Stable Upconversion Nanoparticles. *ACS Appl.*

Nano Mater. **2021**, *4* (4), 4208–4215. https://doi.org/10.1021/acsanm.1c00657.

(21) Lu, Z.; Li, Y.; Qiu, W.; Rogach, A. L.; Nagl, S. Composite Films of CsPbBr 3 Perovskite Nanocrystals in a Hydrophobic Fluoropolymer for Temperature Imaging in Digital Microfluidics. *ACS Appl. Mater. Interfaces* **2020**, *12* (17), 19805–19812. https://doi.org/10.1021/acsami.0c02128.

(22) Runowski, M.; Woźny, P.; Stopikowska, N.; Martín, I. R.; Lavín, V.; Lis, S. Luminescent Nanothermometer Operating at Very High Temperature—Sensing up to 1000 K with Upconverting Nanoparticles (Yb 3+ /Tm 3+). *ACS Appl. Mater. Interfaces* **2020**, *12* (39), 43933–43941. https://doi.org/10.1021/acsami.0c13011.

(23) Chen, Y.; Tran, T. N.; Duong, N. M. H.; Li, C.; Toth, M.; Bradac, C.; Aharonovich, I.; Solntsev, A.; Tran, T. T. Optical Thermometry with Quantum Emitters in Hexagonal Boron Nitride. *ACS Appl. Mater. Interfaces* **2020**, *12* (22), 25464–25470. https://doi.org/10.1021/acsami.0c05735.

(24) *Spin-Crossover Materials: Properties and Applications*; Halcrow, M. A., Ed.; John Wiley & Sons Ltd: Oxford, UK, 2013. https://doi.org/10.1002/9781118519301.

(25) Senthil Kumar, K.; Ruben, M. Emerging Trends in Spin Crossover (SCO) Based Functional Materials and Devices. *Coordination Chemistry Reviews*. Elsevier B.V. September 1, 2017, pp 176–205. https://doi.org/10.1016/j.ccr.2017.03.024.

(26) Bousseksou, A.; Molnár, G. The Spin-Crossover Phenomenon: Towards Molecular Memories. *Comptes Rendus Chim.* **2003**, *6* (8–10), 1175–1183. https://doi.org/10.1016/j.crci.2003.08.011.

(27) Gütlich, P.; Goodwin, H. A. Spin Crossover—An Overall Perspective; 2012; Vol. 1, pp 1–47. https://doi.org/10.1007/b13527.

(28) Salmon, L.; Molnár, G.; Zitouni, D.; Quintero, C.; Bergaud, C.; Micheau, J. C.; Bousseksou, A. A Novel Approach for Fluorescent Thermometry and Thermal Imaging Purposes Using Spin Crossover Nanoparticles. *J. Mater. Chem.* **2010**, *20* (26), 5499–5503. https://doi.org/10.1039/c0jm00631a.

(29) Kraieva, O.; Quintero, C. M.; Suleimanov, I.; Hernandez, E. M.; Lagrange, D.; Salmon, L.; Nicolazzi, W.; Molnár, G.; Bergaud, C.; Bousseksou, A. High Spatial Resolution Imaging of Transient Thermal Events Using Materials with Thermal Memory. *Small* **2016**, *12* (46), 6325–6331. https://doi.org/10.1002/smll.201601766.

(30) Nandi, S. K.; Puyoo, E.; Nath, S. K.; Albertini, D.; Baboux, N.; Das, S. K.; Ratcliff, T.; Elliman, R. G. High Spatial Resolution Thermal Mapping of Volatile Switching in NbO x -Based Memristor Using In Situ Scanning Thermal Microscopy. *ACS Appl.*

Mater. Interfaces **2022**, *14* (25), 29025–29031. https://doi.org/10.1021/acsami.2c06870.

(31) Ridier, K.; Bas, A. C.; Zhang, Y.; Routaboul, L.; Salmon, L.; Molnár, G.; Bergaud, C.; Bousseksou, A. Unprecedented Switching Endurance Affords for High-Resolution Surface Temperature Mapping Using a Spin-Crossover Film. *Nat. Commun.* **2020**, *11* (1), 1–9. https://doi.org/10.1038/s41467-020-17362-7.

(32) Horniichuk, O. Y.; Ridier, K.; Molnár, G.; Kotsyubynsky, V. O.; Shova, S.; Amirkhanov, V. M.; Gural'skiy, I. A.; Salmon, L.; Bousseksou, A. Solvatomorphism, Polymorphism and Spin Crossover in Bis[Hydrotris(1,2,3-Triazol-1-Yl)Borate]Iron(<scp>ii</Scp>). *New J. Chem.* **2022**, *46* (24), 11734–11740. https://doi.org/10.1039/D2NJ01471H.

(33) Hughes, B. C.; Lu, Z.; Jenkins, D. M. The Final Unadorned Tris(Azolyl)Borate: Finishing What Trofimenko Started in 1966. *Chem. Commun.* **2014**, *50* (40), 5273–5275. https://doi.org/10.1039/C3CC47151A.

(34) Quintero, C. M.; Kraieva, O.; Carcenac, F.; Lagrange, D.; Yaremchuk, N. A.; Molnár, G.; Bergaud, C. Joule Heated Metallic Microwire Devices for Sub-Microsecond T-Jump Experiments. *Microelectronics J.* **2015**, *46* (12), 1167–1174. https://doi.org/10.1016/j.mejo.2015.06.024.

(35) Shalabaeva, V.; Rat, S.; Manrique-Juarez, M. D.; Bas, A.-C.; Vendier, L.; Salmon, L.; Molnár, G.; Bousseksou, A. Vacuum Deposition of High-Quality Thin Films Displaying Spin Transition near Room Temperature. *J. Mater. Chem. C* **2017**, *5* (18), 4419–4425. https://doi.org/10.1039/C7TC00999B.

(36) Langford, J. I.; Wilson, A. J. C. Scherrer after Sixty Years: A Survey and Some New Results in the Determination of Crystallite Size. *J. Appl. Crystallogr.* **1978**, *11* (2), 102–113. https://doi.org/10.1107/S0021889878012844.

(37) Ridier, K.; Bas, A.; Shalabaeva, V.; Nicolazzi, W.; Salmon, L.; Molnár, G.; Bousseksou, A.; Lorenc, M.; Bertoni, R.; Collet, E.; Cailleau, H. Finite Size Effects on the Switching Dynamics of Spin-Crossover Thin Films Photoexcited by a Femtosecond Laser Pulse. *Adv. Mater.* **2019**, *31* (25), 1901361. https://doi.org/10.1002/adma.201901361.

(38) Li, D.; Tong, Y.; Bairagi, K.; Kelai, M.; Dappe, Y. J.; Lagoute, J.; Girard, Y.; Rousset, S.; Repain, V.; Barreteau, C.; Brandbyge, M.; Smogunov, A.; Bellec, A. Negative Differential Resistance in Spin-Crossover Molecular Devices. *J. Phys. Chem. Lett.* **2022**, *13* (32), 7514–7520. https://doi.org/10.1021/acs.jpclett.2c01934.

(39) Gavara-Edo, M.; Córdoba, R.; Valverde-Muñoz, F. J.; Herrero-Martín, J.; Real, J. A.; Coronado, E. Electrical Sensing of the Thermal and Light-Induced Spin Transition in Robust Contactless Spin-Crossover/Graphene Hybrid Devices. *Adv. Mater.* **2022**, *34* (33), 2202551. https://doi.org/10.1002/adma.202202551.

(40) Konstantinov, N.; Tauzin, A.; Noumbé, U. N.; Dragoe, D.; Kundys, B.; Majjad, H.; Brosseau, A.; Lenertz, M.; Singh, A.; Berciaud, S.; Boillot, M.-L.; Doudin, B.; Mallah, T.; Dayen, J.-F. Electrical Read-out of Light-Induced Spin Transition in Thin Film Spin Crossover/Graphene Heterostructures. *J. Mater. Chem. C* **2021**, *9* (8), 2712–2720. https://doi.org/10.1039/D0TC05202G.

(41) Boix-Constant, C.; García-López, V.; Navarro-Moratalla, E.; Clemente-León, M.; Zafra, J. L.; Casado, J.; Guinea, F.; Mañas-Valero, S.; Coronado, E. Strain Switching in van Der Waals Heterostructures Triggered by a Spin-Crossover Metal–Organic Framework. *Adv. Mater.* **2022**, *34* (11), 2110027. https://doi.org/10.1002/adma.202110027.

Table of Contents Graphic

